



BSc Thesis Advanced Technology

Observer-based localization and control of an untethered magnetic microrobot

Joep. E. van Seeventer

Examination committee:
dr. I.S.M. Khalil, (Islam)
prof.dr.ir. L. Abelman, (Leon)
dr. D. Makarov, (Denys)

August, 2022

CONFIDENTIAL
Document number: BE-894
Department of Biomedical Engineering
Faculty of Engineering Technology

Abstract—Wireless magnetic control of untethered magnetic devices (UMDs)—such as micro- and milli-robots—using permanent-magnet robotic systems has the potential to change minimally invasive surgery (MIS). These systems work by robotically moving rotating permanent magnets (RPMs) enabling control of UMDs in bodily fluids for targeted therapy. In this thesis, a novel noninvasive magnetic localization and actuation method is proposed and investigated theoretically, numerically and experimentally. The proposed localization method determines the position of UMDs (i.e., milli-rollers) in permanent magnetic coupling using the detected magnetic torque on the RPM actuator. First, a Simulink model is created with the dynamics of the system and an observer is designed to determine the magnetic torque caused by the UMD’s motion with respect to the RPM actuator. Then, the point dipole approximation of the magnetic coupling and the kinematics of the permanent-magnet robotic system are used to estimate the position of the UMD. Then, the Simulink model of the dynamics of the system is tuned and validated by experimental results. The results show that the torque can be estimated successfully and agrees with the theoretical model often used to describe a torque. A 12-mm UMD was also successfully actuated and localized at a distance ranging from 100 to 200 mm from the RPM both numerically and experimentally, with mean average absolute position errors of 3.4 ± 3.3 mm and 6.6 ± 4.5 mm. Finally, 1-D closed-loop control was successfully implemented in the Simulink model.

I. INTRODUCTION

MINIMALLY invasive surgery requires fewer cuts, or incisions than open surgery [1]. Compared to open surgery, the use of MIS is associated with fewer postoperative complications, shorter hospital stay and quicker recovery [1], [2], [3]. This has resulted in an increase of MIS over the last decades and a demand for new minimally invasive surgical technologies [2], [4].

One promising MIS technology in development is magnetic microrobots. UMDs range in size from micrometers to millimeters, allowing them to reach locations in the human body that are otherwise only reachable using open surgery. Untethered and wireless microrobots have the added benefit that they can navigate through natural pathways within the body without obstructing or damaging them and without the need for incisions in some cases. Applications for surgical microrobots include targeted drug delivery, material removal, controllable micro-structures, and telemetry [5].

There are multiple types of microrobots, each differing in type of power source, locomotion method and localization method. Magnetic microrobots have the benefit that low-intensity field strengths do not interact with human tissue, making them a viable option for biomedical applications [6]. Externally powered magnetic microrobots rely on wireless manipulation systems that include power, electronic, electromechanical and localization systems. This enables for a simpler design of UMDs such as a helical wire connected to a magnetic dipole, which can achieve locomotion through rotation. Alternatively, locomotion can be achieved using a tumbling or rolling motion. The design of the UMD depends on the biomedical application.

The integration of wireless actuation of UMDs enabled the integration of open-loop [7], [8], [9] and closed-loop [10] position control during *in vitro* experiments. Due to the fact that their localization method relies on visual feedback to control the position of the UMDs, closed loop *in vivo* applications are not possible with these methods, as body tissues obstruct the microrobot and make localization therefore impossible.

Thus, while the UMD can be simplified for externally powered applications and has yielded promising results *in vitro*, the wireless actuation and localization systems often become too complex for *in vivo* applications. This complexity is caused by the lack of integration of current noninvasive medical imaging technologies. There are two approaches to tackle this problem.

The first approach relies on additional features that can be incorporated into existing imaging technologies. This approach has yielded promising results using existing technologies such as computed tomography [11], ultrasound [12] and photoacoustic [13]. Niedert *et al.* have implemented position control of a tumbling micro-robot using ultrasound imaging both *in vitro* and *in vivo* [14]. Drawbacks of ultrasound include a low signal-to-noise ratio, artifacts that distort or shield the signal due to strong wave reflectors such as bones or air pockets and a low resolution [5]. Pane *et al.* have demonstrated feedback control using a noninvasive localization strategy based on ultrasound acoustic phase analysis inside a tissue-mimicking phantom [15].

The second approach, relying on either on-board magnetic-field sensors or additional sensors within the workspace [16], has been implemented in multiple *in vitro* experiments. Popek *et al.* have demonstrated *in vitro* simultaneous localization and closed-loop position control of a UMD containing embedded Hall-effect sensors using a single RPM as actuator [17]. This method is limited to biomedical applications inside lumen pathways with relatively large diameters, as UMDs with embedded Hall-effect sensors are relatively large and are harder to miniaturize than UMDs with external localization methods. External arrays of magnetic field sensors (1D, 2D or 3D) have been used to achieve actuation and localization of UMDs *in vitro* [18], [19], [20]. A problem associated with Hall-effect sensors is their saturation due to the actuation field, reducing the localization performance.

In this thesis, a new noninvasive localization method for UMDs is proposed and tested both numerically in Simulink and experimentally. The proposed method relies on the estimation of the magnetic coupling between the UMD and the actuator RPM. Through the pose, electric current, angular velocity and angle of the RPM, the position of the UMD can be estimated, allowing simultaneous actuation, localization and control without the need of additional sensors. The influence of multiple actuation and localization parameters (i.e. disturbance observer gain g , gap width p_z , actuation frequency Ω_{act} and the localization algorithm) on the localization performance are

investigated and optimized where possible through simulations and experiments. The experiments and simulations are conducted using a spherical milli-roller for simplicity, but the localization method is not constricted to other types of UMDs that use magnetic torque as propulsion method, see figure 1.

The paper is organized as follows: Section II provides the theoretical background in terms of magnetic forces and torques for the magnetic coupling between the UMD and the RPM, and provides the theoretical conditions for magnetic coupling. Then, using the differential equations for the DC-motor that actuates the RPM, the equations describing the disturbance torque observer are provided. Combining the equations discussed theretofore gives the objective function for localization. Finally, the equations of motion are provided to create a Simulink model that combines the UMD dynamics, RPM dynamics, magnetic coupling, disturbance observer, and localization into a single model. In section III, the design of the DOB is discussed and the experimental and numerical results of the DOB are provided. In section IV, the Simulink model is tuned for multiple actuation frequencies and gap distances. Then, the localization performance is presented both experimentally and using simulations. Section V provides the results of a case of 1D closed-loop position control using the proposed localization method. Practical limitations, suggestions and other comments are provided in section VI. A conclusion to the thesis is given in section VII.

II. THEORY

For the purpose of explaining the theory behind magnetic coupling, both the RPM and the UMD (any micro-robot consisting of a permanent magnet) are considered to be dipole moments. This is accurate as long as the orientation of the UMD and RPM are synchronized.

A. Permanent magnetic coupling interactions

Consider the dipole moments $\mathbf{m} \in \mathbb{R}^3$ and $\mathbf{M} \in \mathbb{R}^3$ for the UMD and RPM respectively. Their positions are defined as $\mathbf{p}_{\text{rob}} \in \mathbb{R}^3$ and $\mathbf{p}_{\text{act}} \in \mathbb{R}^3$ with respect to a reference frame $\{x, y, z\}$.

Defining \mathbf{p} as the position of the UMD with respect to the RPM gives $\mathbf{p} = \mathbf{p}_{\text{rob}} - \mathbf{p}_{\text{act}}$. The magnetic field at the position of the UMD caused by the dipole moment \mathbf{M} of the RPM can be approximated with [21]

$$\mathbf{B}(\mathbf{p}, \mathbf{M}) = \frac{\mu_0}{4\pi} \left(\frac{3\mathbf{p}\mathbf{p}^T}{\|\mathbf{p}\|^5} - \frac{\mathbb{I}}{\|\mathbf{p}\|^3} \right) \mathbf{M}, \quad (1)$$

where $\mu_0 = 4\pi \times 10^{-7} \text{ N}\cdot\text{A}^{-2}$ is the permeability of free space. A similar equation can be constructed for the magnetic field at any position caused by the dipole moment of the UMD. When the UMD is in the vicinity of the RPM, it experiences a magnetic force $\mathbf{F}_m = (\mathbf{m} \cdot \nabla)\mathbf{B}(\mathbf{p}, \mathbf{M})$ [22], which can be further expressed as

$$\mathbf{F}_m = \frac{3\mu_0}{4\pi\|\mathbf{p}\|^4} (\mathbf{M}\mathbf{m}^T + \mathbf{m}\mathbf{M}^T + (\mathbf{m}^T\mathbf{Z}\mathbf{M})\mathbf{I}) \hat{\mathbf{p}}, \quad (2)$$

where $\mathbf{Z} = \mathbf{I} - 5\hat{\mathbf{p}}\hat{\mathbf{p}}^T$ and $\hat{\mathbf{p}}$ is the normalized position. Similarly, the UMD experiences a magnetic torque when in the

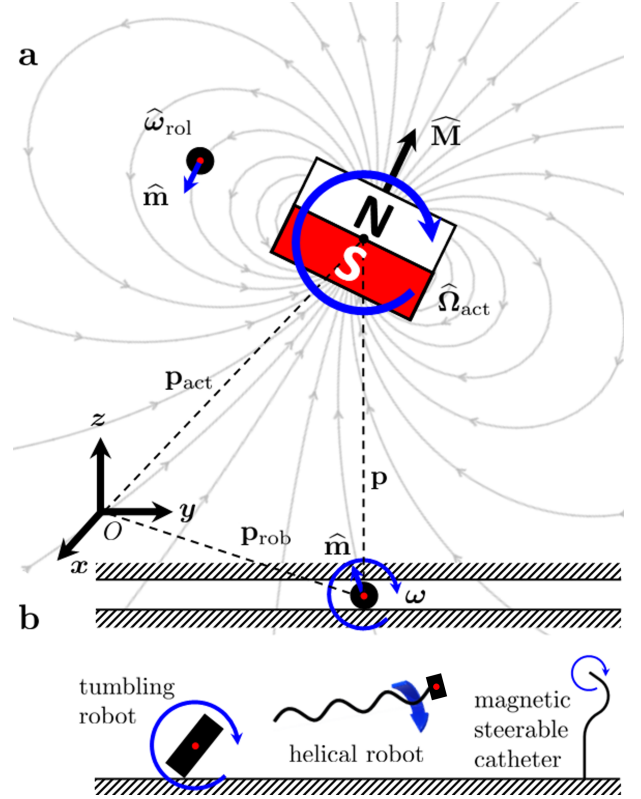


FIG. 1: A magnetic dipole of the rotating permanent magnet (RPM), represented by $\hat{\mathbf{M}}$, produces magnetic field on a dipole moment $\hat{\mathbf{m}}$ of a nearby UMD. The field of the RPM allows wireless locomotion of the UMD, while the coupling between them enables localization. (a) The RPM and the UMD rotate about the axes $\hat{\Omega}_{\text{act}}$ and $\hat{\Omega}_{\text{rol}}$ (out of the page), respectively. Location of the milli-roller and the RPM are characterized by \mathbf{p}_{rob} and \mathbf{p}_{act} with respect to the reference frame $\{x, y, z\}$, respectively. (b) Other types of magnetic torque-propulsed UMDs for which the proposed localization method can be implemented.

vicinity of the RPM. The magnetic torque can be approximated as [22]

$$\mathbf{T}_m = \mathbf{m} \times \mathbf{B}(\mathbf{p}, \mathbf{M}) \quad (3)$$

Together, equation (2) and (3) describe the magnetic coupling between the UMD and the RPM.

Magnetic coupling implies that dipole moments of the UMD and RPM are aligned at all times with a phase lag ϕ and is only possible when the RPM rotates with a rotational velocity Ω_{act} below the step-out frequency Ω_c . The phase lag and step-out frequency can be expressed respectively as [23]

$$\phi = \sin^{-1} \left(\frac{\kappa\eta V \Omega_{\text{act}}}{mB(\mathbf{p}, \mathbf{M})} \right) \quad \Omega_c = \frac{mB(\mathbf{p}, \mathbf{M})}{\kappa\eta V}, \quad (4)$$

where κ is the shape factor, which for a sphere is equal to 6, η is the dynamic viscosity of the lumen, V is the volume of the sphere, m is the magnetic dipole moment of the sphere and $B(\mathbf{p}, \mathbf{M})$ is the magnetic field strength at the position \mathbf{p} .

From equations (2), (3) and (4) it can be concluded that the magnetic force on the UMD scales with $\|\mathbf{p}\|^{-4}$ and that the magnetic torque and the step-out frequency both scale with $\|\mathbf{p}\|^{-3}$. This allows the magnetic force to be neglected at larger distances, as it decreases with one more order of magnitude over distance than the magnetic torque.

B. Disturbance interaction and estimation

The RPM consists of a permanent magnet rigidly connected to the DC-motor. This results in the magnetic torque experienced by the RPM being transferred to the DC-motor as a disturbance torque, which results in a deviation in current and rotational velocity. The differential equation of the RPM subject to a disturbance torque T_{dis} in the mechanical domain can be approximated as

$$(J_1 + J_2) \frac{d\Omega}{dt} + B\Omega = K_t I(t) - T_{\text{dis}}, \quad (5)$$

where J_1 is the rotational inertia of the rotor, J_2 is the rotational inertia of the RPM, B is the viscous friction coefficient, $I(t)$ is the current and K_t is the motor constant. The motor velocity is controlled in a closed feedback loop with a PI-controller with the transfer function $C(s)$. The differential equation of the DC-motor in the electrical domain is

$$L \frac{dI}{dt} + RI(t) = V(t) - \varepsilon(t), \quad (6)$$

where L is the inductance of the motor coil winding, R is the resistance in the winding, $V(t)$ is the supply voltage and $\varepsilon(t)$ is the electromotive force, which is equal to $K_t \Omega$.

Combining equation (5) with (6) and the closed-loop controller gives the transfer function

$$\Omega = \frac{P(s)C(s)}{1 + P(s)(C(s) + K_t)} \Omega_{\text{des}} - \frac{P_m(s)}{1 + P(s)(C(s) + K_t)} T_{\text{dis}}, \quad (7)$$

where $P(s)$ is the transfer function of the electrical and the mechanical plant, $P_m(s)$ is the transfer function of the mechanical plant and Ω_{des} is the setpoint for the rotational velocity of the motor. From (7) it can be concluded that the disturbance torque directly influences the current through the motor and the rotational velocity of the motor.

To estimate the disturbance torque, a disturbance observer (DOB) was implemented. Its block diagram is shown in figure 2 and its equation is given with [24]

$$T_{\text{est}} = \frac{g}{s + g} (K_t I(s) + Jg\Omega) - Jg\Omega, \quad (8)$$

where g is the cut-off frequency of the DOB and J the combined rotational inertia of the motor.

C. Localization using disturbance estimation

To estimate the position of the UMD, the estimated disturbance torque from equation (8) and the theoretical equation for the magnetic torque from equation (3) are combined to achieve the objective function

$$\epsilon = \min_{\mathbf{p}} \left\{ \left\| \mathbf{T}_{\text{est}} - \frac{\mu_0}{4\pi} \mathbf{M} \times D(\mathbf{p}, \mathbf{m}) \right\|^2 \right\}, \quad (9)$$

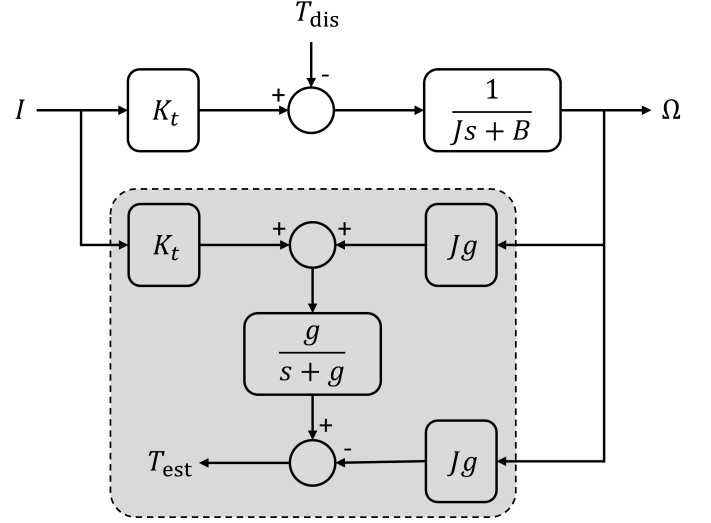


FIG. 2: Block diagram of the disturbance observer (within the shaded area) with current I and rotational velocity Ω as input and estimated disturbance torque T_{est} as output.

where \mathbf{T}_{est} is obtained using the pose \mathbf{q} of the serial manipulator. The pose of the serial manipulator is assumed to be known at all times, as it can be directly and accurately controlled through RoboDK.

After the minimization of (9), the error between the localized position $\hat{\mathbf{p}}$ and the actual position \mathbf{p} can be further reduced by taking the moving average (MVA) of the localized position. The number of previous samples n used for the MVA filter strongly influences the increased performance. The optimal value for n is discussed in section III-A.

D. Dynamics of the UMD and implication in the numerical model

The equations of motion for a spherical microrobot submerged in viscous fluid on a flat surface can be characterized in the low- Re regime using the following force and torque balances [22]

$$\mathbf{F}_m + \mathbf{F}_c + \mathbf{F}_d = 0, \quad (10)$$

where \mathbf{F}_m is the magnetic force as defined in equation (2), \mathbf{F}_c is the contact force due to friction between the roller and the wall and \mathbf{F}_d is the viscous drag force on the UMD. \mathbf{F}_c is the difference between the gravitational and buoyant force, which can be expressed as

$$\mathbf{F}_c = -\mu_f \left(Mg - \frac{4}{3}\pi\rho g R^3 \right) \hat{\mathbf{v}}, \quad (11)$$

where μ_f is the dynamic friction coefficient, M the mass of the sphere, g the gravitational constant, ρ the density of the sphere, R the radius of the sphere and $\hat{\mathbf{v}}$ the normalized velocity of the sphere. The viscous drag force can be approximated as

$$\mathbf{F}_d = 6\pi\eta R (f_t \mathbf{v} + f_r R\Omega), \quad (12)$$

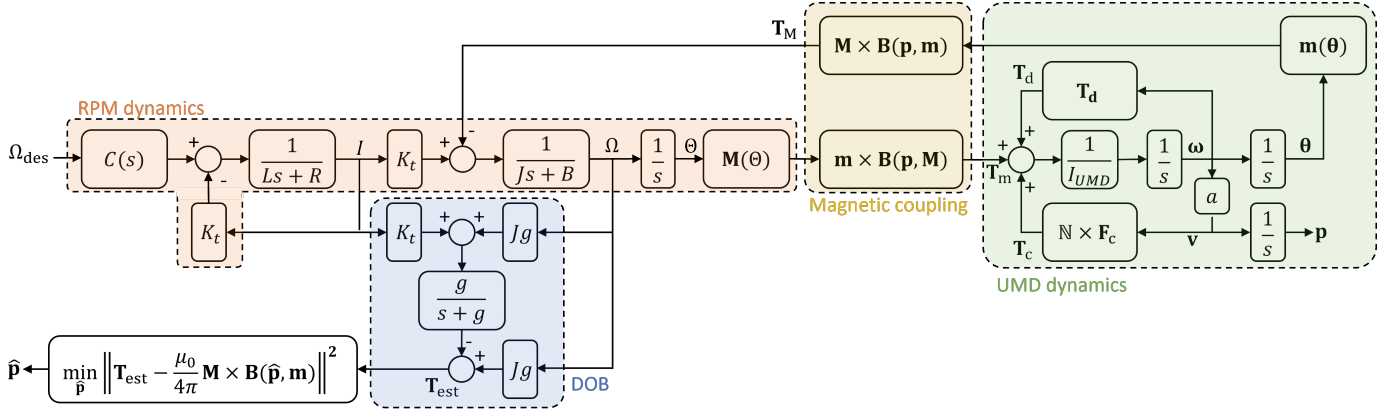


FIG. 3: Simplified block diagram of the model implemented in Simulink based on equations (1)-(15). Not every input is shown for each block, but they can be derived from the equations.

where f_t and f_r are the normalized scalar near-wall fluid forces in the translational and rotational domain respectively, and are given by [25]

$$f_t = \frac{8}{15} \ln\left(\frac{\delta}{R}\right) - 0.959, \quad f_r = \frac{-2}{15} \ln\left(\frac{\delta}{R}\right) - 0.253, \quad (13)$$

where δ is the thickness of the liquid film between the wall and the sphere. The torque balance is [22]

$$\mathbf{T}_m + \mathbf{T}_d + (\mathbb{N} \times \mathbf{F}_c) = 0, \quad (14)$$

where \mathbf{T}_m is the magnetic torque as defined in equation (3), \mathbf{T}_d is the viscous drag torque and \mathbb{N} is the unit vector normal to the plane of motion. The viscous drag torque is given with

$$\mathbf{T}_d = 8\pi\eta R^2 (T_t \mathbf{v} + T_r R \boldsymbol{\Omega}) \quad (15)$$

where T_t and T_r and the normalized scalar near-wall fluid forces in the translational and rotational domain respectively, and are given by [25]

$$T_t = \frac{-1}{10} \ln\left(\frac{\delta}{R}\right) - 0.189, \quad T_r = \frac{2}{5} \ln\left(\frac{\delta}{R}\right) - 0.3817. \quad (16)$$

Combining the equations and transfer functions from this section and section II-B, a model was created in Simulink. A simplified version of the model is shown in figure 3. In the Simulink model, the forces acting on the UMD from (10) are neglected, as the resulting forces from the magnetic torque are significantly larger during applications. A no-slip condition was implemented in the simulation to describe the rolling motion of the sphere, but this condition was tuned during the validation of the model, see section IV-A.

III. TORQUE ESTIMATION

A. Disturbance observer and MVA design

To achieve an accurate estimation of T_m , an optimal value for the observer cut-off frequency g is a requisite. A small g results in little noise, which is desirable, but also increases the phase lag significantly and results in an attenuated output signal if the cut-off frequency is below the actuation frequency. On the other hand, a large value for g passes more noise through the filter but decreases the phase lag and attenuation.

Since any error between the estimated torque and T_m results in a propagated error during localization, the optimal value for g can be found through the minimization algorithm output.

The output of the minimization algorithm has a jittering artifact—see figure 10—that increases the localization error. A moving average filter reduces jittering in the output of the minimization algorithm. The jittering artifact can be reduced by using the smooth function provided by MATLAB. The smooth function calculates the moving average at sample i using the n previous samples. A large n will remove the artifact entirely but attenuate the signal as well. A small n removes less jittering but will attenuate less.

To find an optimal combination of g and n , the localization error during the experiment shown in figure 7 was simulated for a large number of combinations of g and n . The results are shown in figure 4. The figure shows that in the region $n \in [90 : 4000]$ and $g > 15$ the localization error decreases with at least 60%.

B. Magnetic torque estimation

The torque estimation was implemented both experimentally and in the simulation. The experimental set-up used for the experiment is shown in figure 5 and consists of a small section of tube with a inner diameter of 15 mm filled with 1000cst silicone oil and a spherical UMD with a diameter of 12 mm. The UMD is constrained in all translational dimensions. The RPM is mounted on a DC-motor and is the end-effector of a 6 degrees of freedom (DOF) serial manipulator. The pose of the serial manipulator is such that the rotation axis of the RPM is perpendicular to the tube.

During this set of experiments, the gap distance was decreased from 125 mm to 40 mm with a velocity v_z of 1, 5, or 20 mm/s. For each velocity v_z the RPM rotates at a rotational velocity Ω of 0.2, 1, 2, or 4 Hz. Each experiment (i.e. 16 in total) was repeated five times. The experimental set-up was recreated in Simulink with the same boundary conditions and simulated once for every combination of v_z and Ω . A part of the results are presented in figure 6. This figure shows a cubic increase of the magnitude of the magnetic torque \hat{T}_m as the gap decreases linearly over time, allowing the localization of the UMD position on the basis of equation (3).

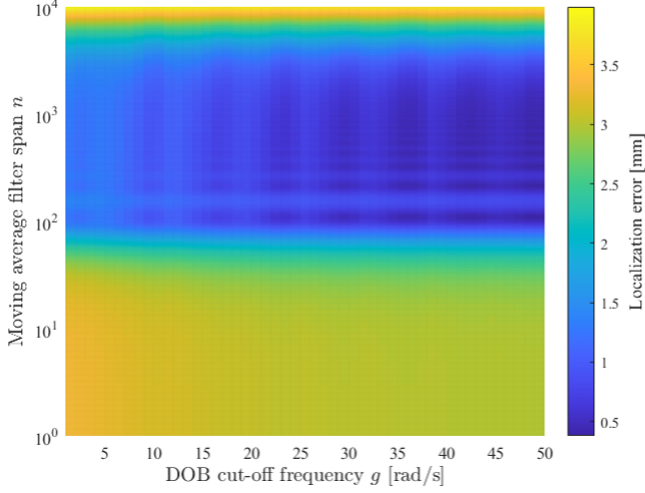


FIG. 4: Localization error as a function of disturbance observer cut-off frequency and moving average filter span. The error is calculated as the mean error between the localized position and the actual position during the simulation of the experiment shown in figure 7. This was done at a gap width of 100 mm and actuation frequency of 2 Hz. The average sampling frequency is 494 Hz.

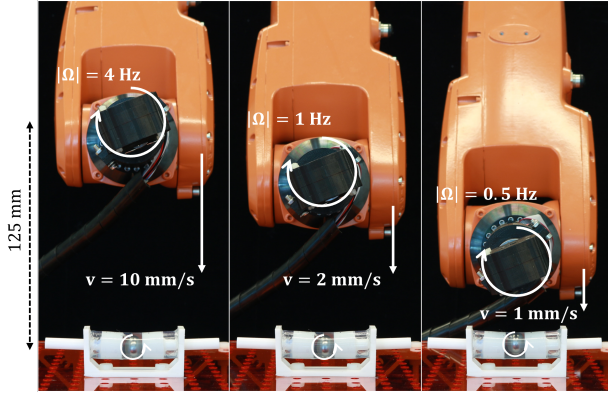


FIG. 5: Magnetic coupling estimation for various rotational velocities $|\Omega| \in [0.2, 1, 2, 4]$ Hz of the RPM and transnational speeds $v_z \in [1, 5, 10, 20]$ mm/s. Each experiment starts with a gap width of 125 mm and ends with a gap width of 40 mm. Each experiment was repeated five times. The transnational velocity of the RPM is controlled during the vertical motion towards the 12 mm UMD while the position of the UMD is fully constrained.

IV. SIMULTANEOUS ACTUATION AND LOCALIZATION

In the previous experiment, the position of the UMD was fully constrained, to show the performance of the disturbance observer. In this section, the results of a different experiment will be presented. This experiment implements both actuation and localization. The UMD is constrained in two dimensions and can now move in the dimension perpendicular to the rotation axis of the RPM. The RPM is now fixed in all dimensions. A longer tube was used and filled with the same 1000cst silicone oil and the same spherical UMD. The

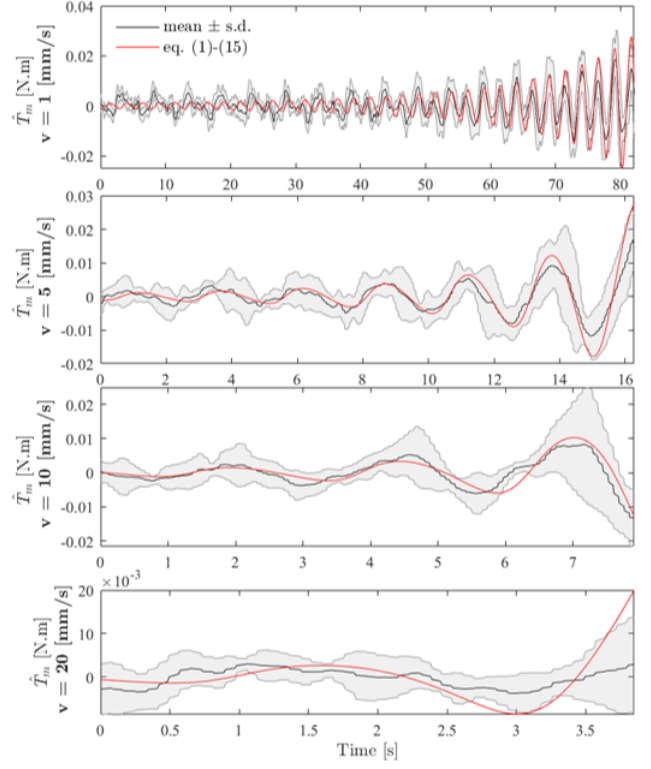


FIG. 6: Magnetic torque estimation as shown in figure 5. The rotational velocity $|\Omega|$ is 0.2 Hz. The UMD is constrained in all translational dimensions while the RPM moves vertically downwards for various speeds $v_z \in [1, 5, 10, 20]$ mm/s. Each experiment was repeated five times.

experimental set-up is shown in figure 7.

The RPM is actuated for 32 seconds at a rotational velocity Ω . The sign of Ω is flipped at $t = 8$ s and $t = 24$ s, such that the UMD is at the same position after the experiment as before the experiment. This experiment was repeated for $\Omega = 0.5, 1, 2$ and 4 Hz and for the multiple gap distances $p_z = 100, 120, 140, 160, 180$ and 200 mm. Each experiment was repeated five times. The experimental set-up was also recreated in Simulink and simulated once for every combination of Ω and p_z .

A. Simulink model validation

Firstly, the goal of the experiment is to tune the model in Simulink. The model was created using the no-slip condition as a model for the rolling motion of the sphere. This is in most applications a valid assumption, as it reduces the complexity of the model and is accurate for low velocities. To determine whether this was a valid assumption, the average mean translational velocity of the UMD v and the rotational velocity of the RPM Ω was determined for each measurement, resulting in table I. Assuming that the orientation of the UMD is in sync with the orientation of the RPM allows Ω to be an approximation of the rotational velocity of the UMD. Using table I, the mean translational velocity at all distances p_z was fitted to the corresponding mean rotational velocity assuming the relationship $v = a\Omega$, where a is the fit parameter. A

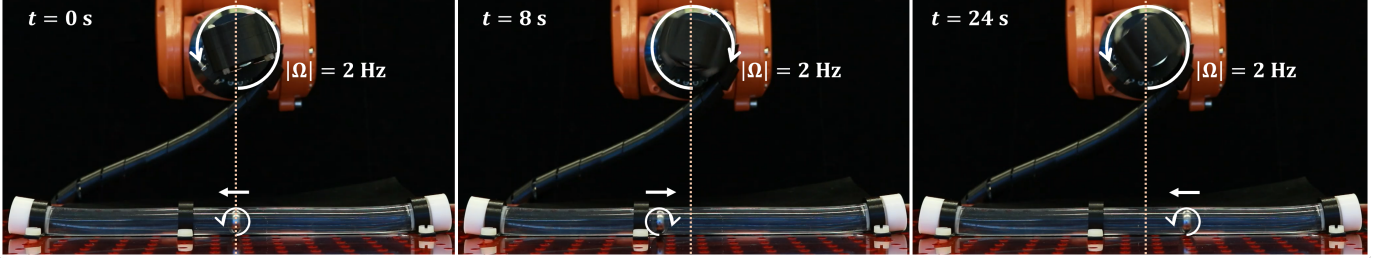


FIG. 7: Simultaneous actuation and localization for various rotational velocities $|\Omega| \in [0.5, 1, 2, 4]$ Hz of the RPM and gap widths $p_z \in [100 : 20 : 200]$ mm. Each experiment was repeated five times. The position of the RPM is fully constrained at all times. The direction of rotation is reversed at $t = 8$ s and at $t = 24$ s resulting in the UMD trajectory resembling a single triangle wave, see figure 8.

no-slip condition would imply that $a = R$, where R is the radius of the sphere. The value of a was found to be equal to $(1.76 \pm 0.095) \times 10^{-4}$ m, implying that the UMD is indeed slipping.

TABLE I: Mean translational velocity v divided by the mean rotational velocity Ω for every measurement.

	$ \Omega = 0.5$ Hz	$ \Omega = 1$ Hz	$ \Omega = 2$ Hz
$p_z = 100$ mm	$2.27 \cdot 10^{-4}$	$2.23 \cdot 10^{-4}$	$1.91 \cdot 10^{-4}$
$p_z = 120$ mm	$2.22 \cdot 10^{-4}$	$1.85 \cdot 10^{-4}$	$1.82 \cdot 10^{-4}$
$p_z = 160$ mm	$1.41 \cdot 10^{-4}$	$1.72 \cdot 10^{-4}$	$1.76 \cdot 10^{-4}$
$p_z = 180$ mm	$1.61 \cdot 10^{-4}$	$1.72 \cdot 10^{-4}$	$1.67 \cdot 10^{-4}$
$p_z = 200$ mm	$1.26 \cdot 10^{-4}$	$1.67 \cdot 10^{-4}$	$1.14 \cdot 10^{-4}$

Since the displacement of the UMD is approximately linear at a constant rotational velocity of the RPM—see figure 8—the no-slip condition in the model was changed to the relation $v = 0.0294 * R\Omega$. This implementation reduces the displacement of the UMD in the simulation, bringing the performance of the model closer to the real world. In table II the mean absolute difference between the simulated position and the mean average error (MAE) of the experimental position are provided for the experiments shown in figure 8. Taking the mean of all experiments from table II gives a mean average error of 1.48 ± 0.97 mm between the experimental and simulated position.

TABLE II: Mean average error between the experimentally tracked position (each repeated five times) and the simulated position after tuning.

	$ \Omega = 0.5$ Hz	$ \Omega = 1$ Hz	$ \Omega = 2$ Hz
$p_z = 100$ mm	$1.09 \cdot 10^{-3}$	$2.71 \cdot 10^{-3}$	$4.63 \cdot 10^{-3}$
$p_z = 120$ mm	$2.11 \cdot 10^{-3}$	$9.52 \cdot 10^{-4}$	$2.08 \cdot 10^{-3}$
$p_z = 160$ mm	$4.38 \cdot 10^{-4}$	$3.58 \cdot 10^{-4}$	$6.03 \cdot 10^{-4}$
$p_z = 180$ mm	$5.51 \cdot 10^{-4}$	$1.22 \cdot 10^{-4}$	$3.36 \cdot 10^{-4}$
$p_z = 200$ mm	$7.36 \cdot 10^{-4}$	$4.46 \cdot 10^{-4}$	$5.07 \cdot 10^{-3}$

B. Localization performance

The second goal of the experiment shown in figure 7 is to test the performance of the localization method for both the simulation and the experiment. The same localization algorithm was implemented for both the experimental results and the simulated results using the built-in `fmincon()`

function in MATLAB. `fmincon()` can find the minimum or maximum of a constrained nonlinear multi-variable objective function. The objective function in this case is equation (9), where p_x and p_z are assumed to be given and constant. The function requires an initial point p_0 from which the minimization starts, which in this case was chosen to be the previously minimized location. The lower and upper bound for the solution were implemented as p_0 minus and plus a small absolute distance δ respectively — it was assumed the rolling motion of the UMD is continuous. No other constraints were given to the function. The value of δ was tuned to result in the smallest possible localization error. One sample of the localization results of the simulated experiment are shown in figure 10, the experimental localization results are shown in figure 9. A summary of both the simulation and experimental results is shown in figure 11 and 12 respectively. The mean average error over all combinations of p_z and $|\Omega|$ of the simulation results in figure 11 is 3.4 ± 3.3 mm. Respectively, the mean average error of the experimental results is 6.6 ± 4.5 mm.

V. CLOSED-LOOP CONTROL IN SIMULINK

The next step after simultaneous actuation and localization is the implementation of feedback control. For this experiment, a PID-controller was implemented to control the position of the UMD in one dimension similar to the actuation of the experiment shown in figure 7. The experiment was conducted only in Simulink and consisted of multiple step-responses for the step heights $p_{\text{set}} \in [1, 5, 10]$ cm. Figure 13 provides the results of the experiment after tuning the PID-controller. The controller was able to follow the reference for $p_{\text{set}} = 1$ and 5 cm using $p_{\text{set}} - \hat{p}_y$ as error.

VI. DISCUSSION

In figure 11, the datapoint of $p_z = 200$ mm and $|\Omega| = 4$ Hz is missing. This was done intentionally, since the UMD is actuated above step-out frequency at this distance. This resulted in the simulation not being able to localize correctly, which gave a localization error several magnitudes larger than the other datapoints. Therefore, considering this case was above step-out frequency, it was left out.

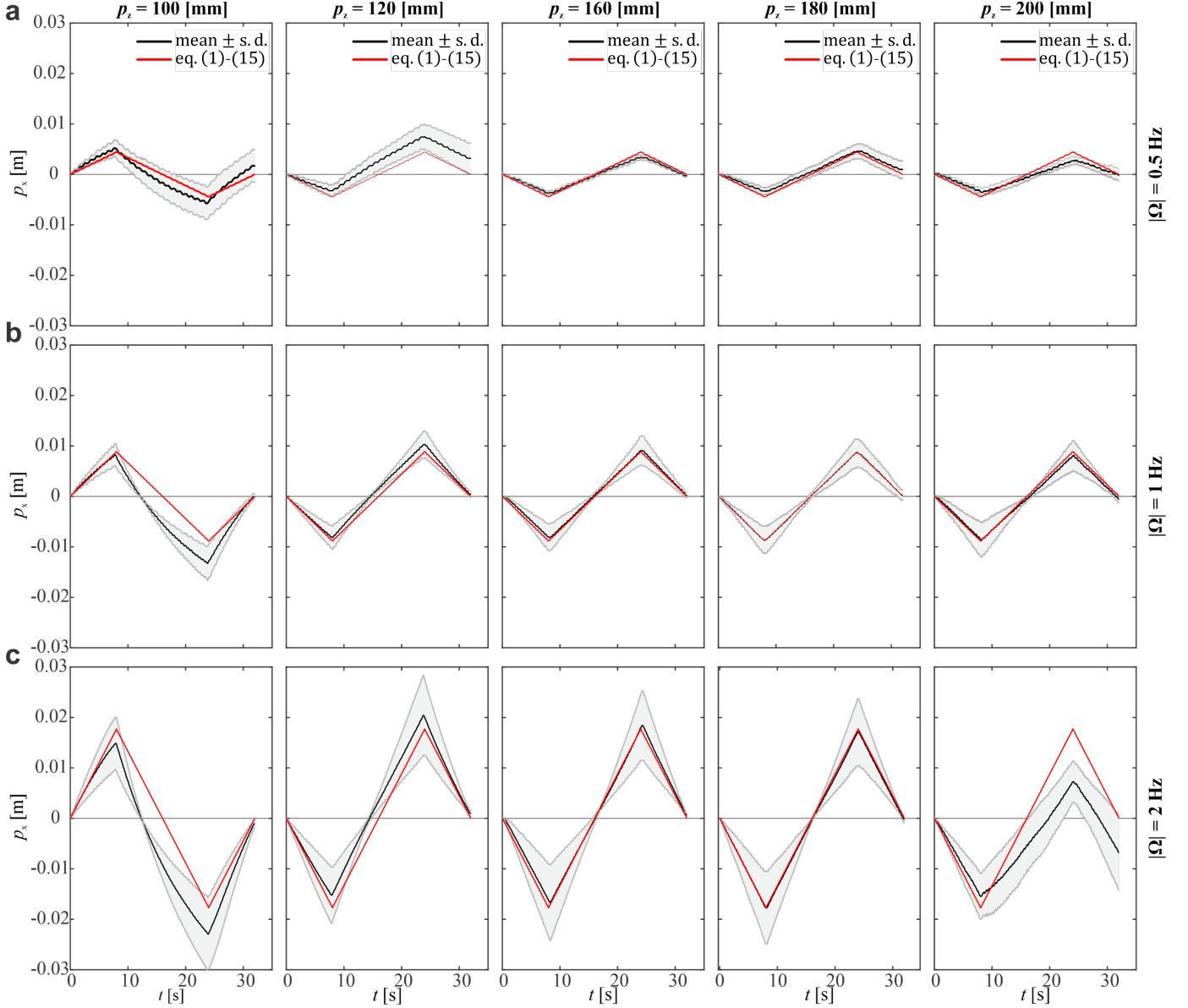


FIG. 8: Comparison of tuned model and experimental results for the experiment shown in figure 7. The UMD is allowed to roll back-and-forth along the y-axis inside the tube. The position of the UMD is tracked to validate tuned model. The RPM was actuated with the rotational velocities $|\Omega| \in [0.5 : 2]$ Hz at various gap widths $p_z \in [100 : 200]$ mm.

In section III-A, a moving average filter to reduce the localization error was discussed. This filter was only implemented for the simulated experiments. It was not implemented in the physical experiments as the reduction of localization error was negligible compared to the effect for the simulated experiments. Figure 4 was created using a gap width of 100 mm and actuation frequency of 2 Hz. Other combinations can result in different regions that decrease the localization error.

The closed-loop control was hand-tuned and does not perform optimally. There are two other problems with a PID-controller that limit the performance of closed-loop control of UMDs. The first problem is that there is no limit to the control effort, resulting in actuation above step-out frequency if the error is too large. Above step-out frequency the UMD does not rotate in sync with the RPM, but it does provide a torque

to the RPM. This reduces the performance of the localization method and can cause the system to diverge. This problem can be partially solved by limiting the control effort below the step-out frequency, but the step-out frequency is dependent on the distance between the UMD and the RPM and can become an unreliable limit if the localization error is too big. A solution could be to control the pose of the robot such that p always is small to ensure a large step-out frequency, which gives rise to new challenges regarding safety and a limited workspace.

The localization method was implemented by minimizing equation (9) for one component of \mathbf{p} , i.e. p_y . As the UMD was allowed to move in one dimension, this was an accurate implementation. To implement this localization method *in vivo*, the localization method must minimize equation (9) for all components of \mathbf{p} , i.e. p_x , p_y and p_z . An attempt was

made to implement a second component of \mathbf{p} , i.e. p_z , into the localization method, but due to an increase in localization error compared to one-component minimization, the localization method was constricted to one-component minimization.

The model in figure 3 is based on the torque balance and does not include forces. Figure 8 shows this is accurate for relatively large gap widths, i.e. larger than 100 mm. As the gap width decreases below 100 mm, the influence of the magnetic force becomes increasingly larger and the model will not be accurate anymore. This has no influence

on the localization process itself as the objective function in equation (9) is independent on any force. However, a future study into the effectiveness of this localization method for smaller microrobots—with radii in the range of or smaller than smaller than 1 mm—could result in smaller localization errors if smaller gap widths can be implemented. Therefore, the implementation of forces into the model are essential if smaller UMDs are required.

A study into smaller UMDs would bring this localization method closer to *in vivo* applications, as a 12 mm UMD is too

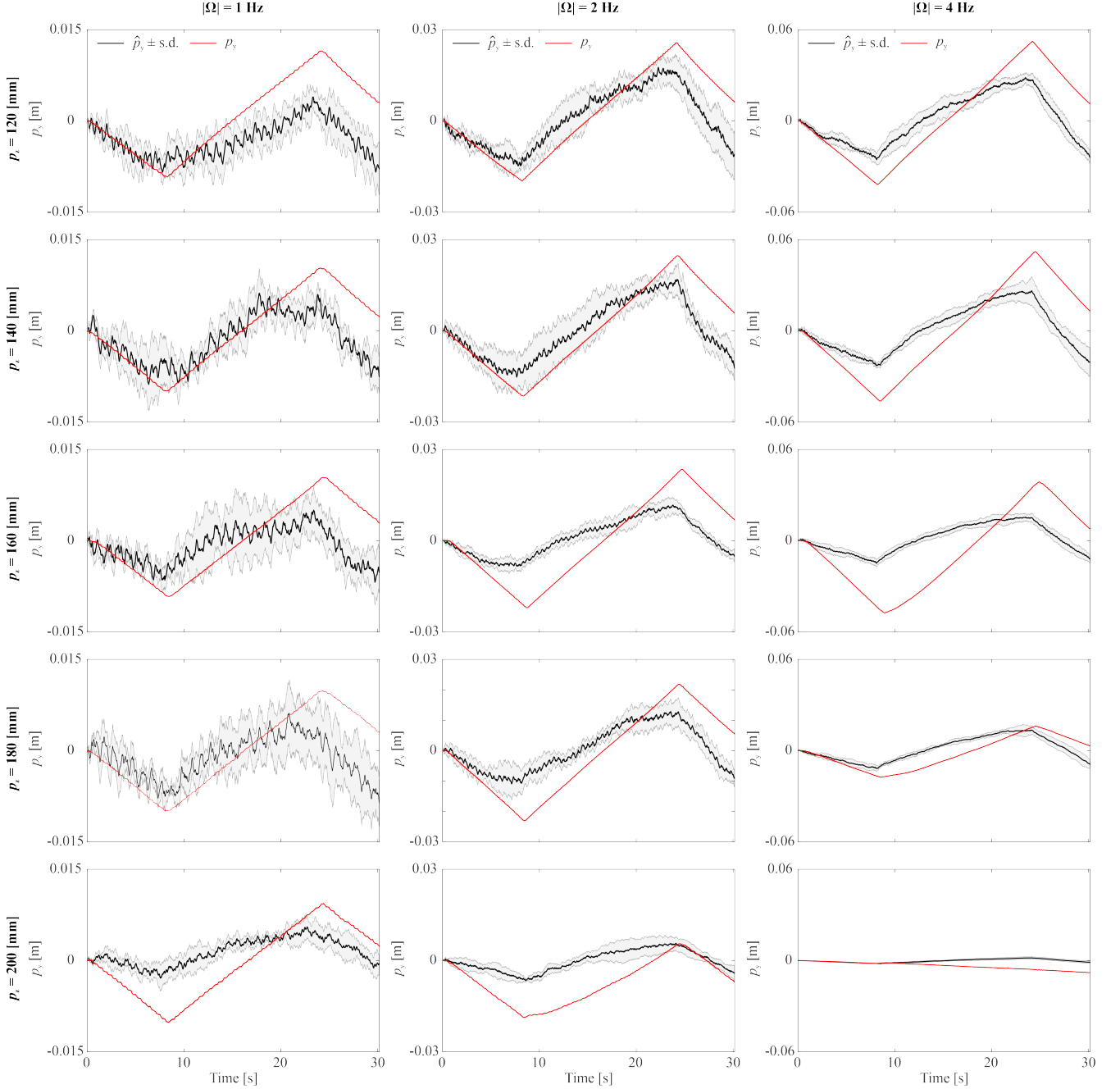


FIG. 9: Experimental results of the localization method for the experiment shown in figure 7. The UMD is allowed to roll back and forth along the y-axis in the tube. The position of the UMD is tracked to validate the localization method. The RPM was actuated with the rotational velocities $|\Omega| \in [1, 2, 4]$ Hz at various gap widths $p_z \in [120 : 200]$ mm. The mean average localization error for all combinations of $|\Omega|$ and p_z are shown in figure 12.

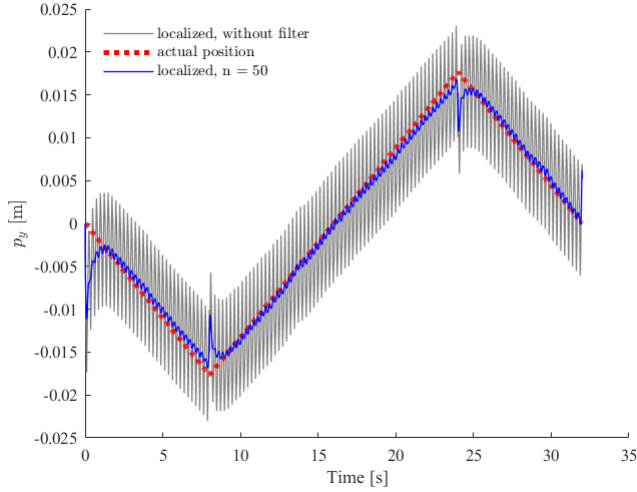


FIG. 10: Localization error as a function of disturbance observer cut-off frequency and moving average filter span. The error is calculated as the error between the localized position and the actual position during the simulation of the experiment shown in figure 7. The simulated gap width is 100 mm and the actuation frequency is 2 Hz. The average sampling frequency is 494 Hz.

big for *in vivo* applications. An attempt was made to create a Simulink model that allows for the implementation of smaller rollers for this thesis, but this attempt was unsuccessful. This was caused by the fact that small UMDs have a small inertia, which results in a very stiff system, which is inherently hard to simulate as it requires very small time-steps—in the order of or smaller than nanoseconds—or often does not converge. That’s why for smaller UMDs a new model has to be created that does not rely on inertia or mass. The construction and validation of such a model was beyond the scope of this thesis.

VII. CONCLUSION

In this thesis, a basic physical framework necessary to implement a noninvasive permanent magnetic coupling localization method is presented that simultaneously actuates and localizes UMDs using a single RPM during 1-D motion in confined environments. On the basis of a magnetic coupling observer, it is shown numerically and experimentally that the error between the actual and estimated torque can be made arbitrarily small, allowing the position of the UMD to be estimated using a quadratic least-squares problem. The simultaneous open-loop actuation and localization of a 12-mm magnetic roller at a distance ranging from 100 to 200 mm from the RPM actuator results in an average error of 3.4 ± 3.3 mm for the simulated model and a mean average error of 6.6 ± 4.5 mm. The measurements show this localization method allows for the implementation of 1-D closed-loop position control of the UMD.

REFERENCES

- [1] “Minimally invasive surgery,” Available at <https://www.healthline.com/health/minimally-invasive-surgery> (24-03-22).

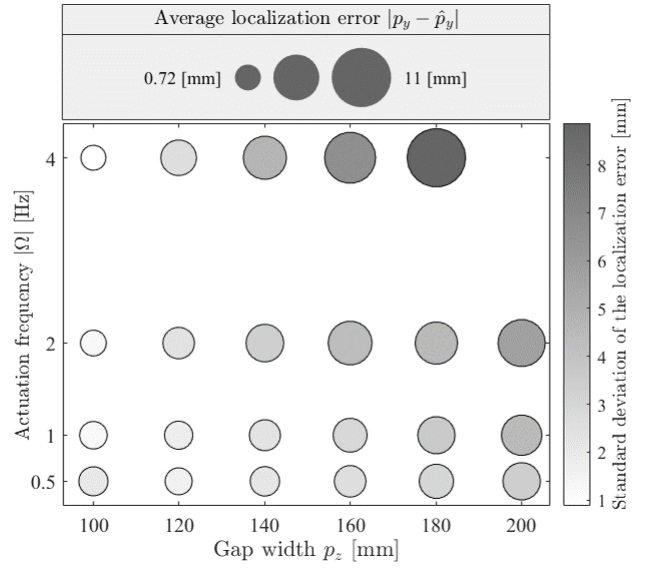


FIG. 11: Simulation results of the average localization error $|p_y - \hat{p}_y|$ with standard deviation for multiple gap widths $p_z \in [100 : 20 : 200]$ and multiple actuation frequencies $|\Omega| \in [0.5, 1, 2, 4]$ Hz. The error is calculated as the average error between the localized position and the actual position during the simulation of the experiment shown in figure 7. The size and the shade of each bubble represents the average localization error and standard deviation respectively.

- [2] R. Tejwani, B. J. Young, and H. S. Wang, “Open versus minimally invasive surgical approaches in pediatric urology: Trends in utilization and complications,” *Journal of pediatric urology*, vol. 13, pp. 283.e1–283.e9, 2017.
- [3] T. Fullum, J. Ladapo, B. Borah, and C. Gunnarsson, “Comparison of the clinical and economic outcomes between open and minimally invasive appendectomy and colectomy: Evidence from a large commercial payer database,” *Surgical Endoscopy*, vol. 24, pp. 845–853, 04 2010.
- [4] A. Hughes-Hallett, E. K. Mayer, P. J. Pratt, J. A. Vale, and A. W. Darzi, “Quantitative analysis of technological innovation in minimally invasive surgery,” *British Journal of Surgery*, vol. 102, no. 2, pp. e151–e157, 01 2015. [Online]. Available: <https://doi.org/10.1002/bjs.9706>
- [5] B. J. Nelson, I. K. Kaliakatos, and J. J. Abbott, “Microrobots for minimally invasive medicine,” *Annual Review of Biomedical Engineering*, vol. 15, pp. 56–60, 08 2010.
- [6] T. Xu, W. Gao, L.-P. Xu, X. Zhang, and S. Wang, “Fuel-free synthetic micro-/nanomachines,” *Advanced Materials*, vol. 29, no. 9.
- [7] R. Avaneesh, R. Venezian, C.-S. Kim, J.-O. Park, S. Misra, and I. S. M. Khalil, “Open-loop magnetic actuation of helical robots using position-constrained rotating dipole field,” *2021 IEEE/RSJ International Conference on Intelligent Robots and Systems (IROS)*, pp. 8545–8550, 2021.
- [8] T. W. R. Fountain, P. V. Kailat, and J. J. Abbott, “Wireless control of magnetic helical microrobots using a rotating-permanent-magnet manipulator,” pp. 576–581, 2010.
- [9] W. Chen, X. Fan, M. Sun, and H. Xie, “The cube-shaped hematite microrobot for biomedical application,” *Mechatronics*, vol. 74, 2021.
- [10] A. W. Mahoney and J. J. Abbott, “Five-degree-of-freedom manipulation of an untethered magnetic device in fluid using a single permanent magnet with application in stomach capsule endoscopy,” *The International Journal of Robotics Research*, vol. 35, no. 1-3, pp. 129–147, 2016.
- [11] A. Hong, A. J. Petruska, and B. J. Nelson, “Tracking a magnetically guided catheter with a single rotating c-arm,” in *Proceedings of the IEEE International Conference on Robotics and Automation (ICRA)*, pp. 618–623, 2015.
- [12] I. S. M. Khalil, D. Mahdy, A. E. Sharkawy, R. R. Moustafa, A. F. Tabak, M. Elwi, S. Hesham, N. Hamdi, A. Klingner, A. Mohamed, and M. Sitti, “Mechanical rubbing of blood clots using helical robots under

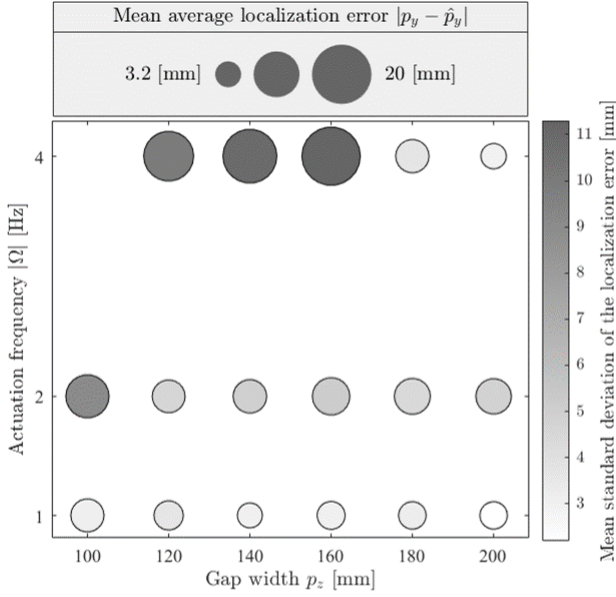


FIG. 12: Experimental results of the average localization error $|p_y - \hat{p}_y|$ with standard deviation for multiple gap widths $p_z \in [100 : 20 : 200]$ and multiple actuation frequencies $|\Omega| \in [1, 2, 4]$ Hz. The error is calculated as the average error between the localized position and the actual position during the experiment shown in figure 7. The size and the shade of each bubble represents the average localization error and standard deviation respectively.

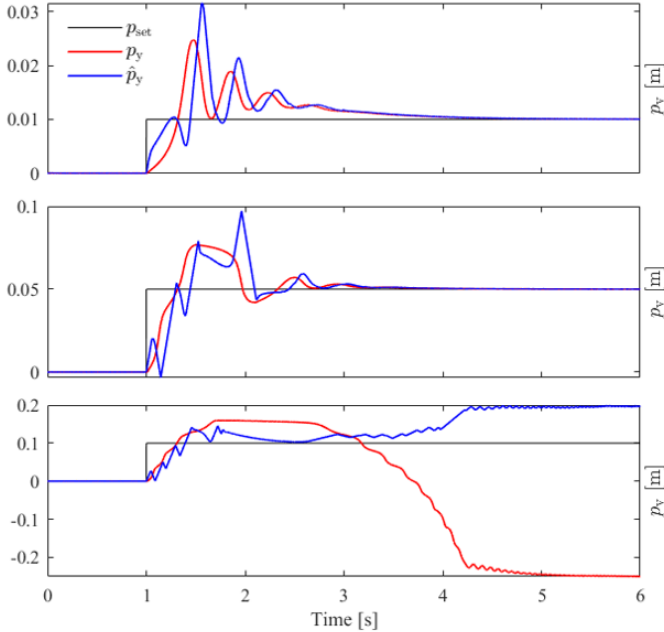


FIG. 13: Multiple simulated step-responses for 1-D position control using PID. The UMD was constrained in all other translational dimensions. Each plot shows the set point p_{set} , the actual position p_y and the estimated position \hat{p}_y . Only \hat{p}_y was used in the control-loop, p_y is shown for reference.

- ultrasound guidance,” *IEEE Robotics Automation Letters (RAL)*, vol. 3, no. 2, pp. 1112–1119, 2018.
- [13] L. V. Wang and J. Yao, “A practical guide to photoacoustic tomography in the life sciences,” *Nat. Methods*, vol. 13, pp. 627–638, 2016.
- [14] E. E. Niedert, C. Bi, G. Adam, E. Lambert, L. Solorio, C. J. Goergen, and D. J. Cappelleri, “A tumbling magnetic microrobot system for biomedical applications,” *Micromachines*, vol. 11, no. 9, 2020.
- [15] S. Pane, G. Faoro, E. Sinibaldi, V. Iacovacci, and A. Menciasci, “Ultrasound acoustic phase analysis enables robotic visual-servoing of magnetic microrobots,” *IEEE Transactions on Robotics*, vol. 38, no. 3, pp. 1571–1582, 2022.
- [16] J. Edelmann, A. J. Petruska, and B. J. Nelson, “Estimation-based control of a magnetic endoscope without device localization,” *Journal of Medical Robotics Research*, 2018.
- [17] K. M. Popek, T. Hermans, and J. J. Abbott, “First demonstration of simultaneous localization and propulsion of a magnetic capsule in a lumen using a single rotating magnet,” *IEEE International Conference on Robotics and Automation (ICRA)*, pp. 1154–1160, 2017.
- [18] C. Hu, M. Li, S. Song, W. Yang, R. Zhang, and M. Meng, “A cubic 3-axis magnetic sensor array for wirelessly tracking magnet position and orientation,” *IEEE Sensors Journal*, vol. 10, no. 5, pp. 903–913, 2010.
- [19] S. Song, B. Li, W. Qiao, C. Hu, H. Ren, H. Yu, Q. Zhang, M. Q.-H. Meng, and G. Xu, “6-d magnetic localization and orientation method for an annular magnet based on a closed-form analytical model,” *IEEE Transactions on Magnetics*, vol. 50, no. 9, 2014.
- [20] D. Son, S. Yim, and M. Sitti, “A 5-d localization method for a magnetically manipulated untethered robot using a 2-d array of hall-effect sensors,” *IEEE/ASME Trans. Mechatronics*, vol. 21, no. 2, pp. 708–716, 2016.
- [21] I. S. Khalil, A. Klingner, and S. Misra, “Chapter 3 - theory of electromagnetics: Soft-magnetic bodies,” in *Mathematical Modeling of Swimming Soft Microrobots*, I. Khalil, A. Klingner, and S. Misra, Eds. Academic Press, 2021, pp. 53–54.
- [22] M. M. Micheal, A. Adel, C.-S. Kim, J.-O. Park, S. Misra, and I. S. M. Khalil, “2d magnetic actuation and localization of a surface milli-roller in low reynolds numbers,” *IEEE Robotics and Automation Letters*, vol. 7, no. 2, pp. 3874–3881, 2022.
- [23] B. H. McNaughton, K. A. Kehbein, J. N. Anker, and R. Kopelman, “Sudden breakdown in linear response of a rotationally driven magnetic microparticle and application to physical and chemical microsensing,” *The Journal of Physical Chemistry B*, vol. 110, no. 38, pp. 18 958–18 964, 2006.
- [24] E. Sariyildiz and K. Ohnishi, “Adaptive reaction torque/force observer design i,” in *2014 IEEE 13th International Workshop on Advanced Motion Control (AMC)*, 2014, pp. 563–568.
- [25] A. Goldman, R. Cox, and H. Brenner, “Slow viscous motion of a sphere parallel to a plane wall—i motion through a quiescent fluid,” *Chemical Engineering Science*, vol. 22, no. 4, pp. 637–651, 1967.